Dynamics slowdown induced by gas oversolubility in nanoconfined fluids

Linh Ngoc Ho, Anne Lesage, Aaron Rossini, David Farrusseng, Benoit Coasne

Dynamics slowdown induced by gas oversolubility in nanoconfined fluids

Linh Ngoc Ho,[1] Anne Lesage,[2] Aaron Rossini,[2,3] David Farrusseng,[1] and Benoit Coasne[4,5,*]

[1] *Université de Lyon, Université Claude Bernard Lyon 1, CNRS, IRCELYON, UMR 5256, Villeurbanne, France*

[2] *Centre de RMN à très Hauts Champs - CRMN, CNRS (UMR 5280)/ENS Lyon/Université Claude Bernard Lyon 1, Villeurbanne, France*

[3] *Department of Chemistry, Iowa State University, 2438 Pammel Drive, Ames, Iowa 50011, United States*

[4] *Univ. Grenoble Alpes, CNRS, LIPhy, 38000 Grenoble, France*

[5] *Institut Laue-Langevin, 71 Avenue des Martyrs, 38042 Grenoble, France*

Abstract

Oversolubility refers to the observation in nanoconfined liquids of significant gas solubilities that largely surpass the bulk solubility. While this thermodynamic effect is now well-documented, its impact on the dynamics of fluids confined in nanoporous materials has not been explored. Yet, by affecting adsorption and wetting at solid/liquid interfaces, oversolubility is expected to be a key phenomenon in separation and catalysis but also in geological applications such as pollutant migration in soils, carbon capture/storage in natural environments, and underground/atmosphere exchanges. Here, we employ atom-scale simulations and NMR experiments to show that gas oversolubility is expected in hydrated nanoporous materials and that it reduces both water and ion diffusivities [by 10% up to 60% depending on thermodynamic conditions]. Despite the complexity of adsorption/transport coupling in such gas/liquid/solid systems, we establish that diffusivities in the presence of small gases such as CO_2, CH_4 and H_2 can be rationalized by accounting for the increase in the confined fluid viscosity (which is found to be directly linked to the decrease in the free volume accessible to the liquid upon solubilization). Moreover, in agreement with the reported data, by invoking Stokes-Einstein relation between the viscosity and diffusivity, we predict that the dynamics slowdown is identical for the confined water molecules and ionic species. We also show that this oversolubility-induced dynamical effect becomes more pronounced as the strength of the molecular interactions between the solubilized gas and the liquid/solid increase. This

*Electronic address: benoit.coasne@univ-grenoble-alpes.fr

approach provides a robust formalism to fluid diffusion in nanoconfined environments subjected to gas solubility and potential oversolubility effects.

Introduction

Confinement and transport of fluids in nanoporous media (pore size $d \sim 1 - 100$ nm [1]) – such as zeolites, metal organic frameworks, and active carbons but also small infractuosities in geological environments (e.g. soils, rocks) – involve complex mechanisms arising from the strength of the fluid/solid molecular interactions and the geometrically-restricted diffusivity in the host structure [2–5]. As a result, depending on the porosity surface to volume ratio $S/V \sim d$ and the range of the intermolecular forces ξ, intriguing phenomena get unravelled regularly with striking coupled adsorption/transport effects (slippage and interfacial transport [2], anomalous diffusion including single-file [6] and stop-and-go diffusion [7], activated transport induced by surface free energy barriers [8], etc). Even when porous materials exhibit multiscale porosity with large pores, transport of gases and liquids confined in their porosity is often driven to a large extent by adsorption phenomena occurring in the smallest porosity scales as they can change locally the component concentration as well as their thermodynamical and dynamical behavior. Deciphering adsorption in nanoporous materials is therefore crucial to predict the diffusion and retention of fluids in their nanoscale porosity with important applications in chemical engineering (adsorption, separation, catalysis), soil science and hydrology (pollutant migration, water remediation), environmental science and global warming mitigation (carbon capture and storage and long-term nuclear waste storage), and atmospheric physical chemistry (gas exchange between the underground and atmosphere through soil porosity) [9, 10].

Among perturbations that drastically affect confinement and transport in nanoporous materials, the physical chemistry of dissolved gases in nanoconfined fluids remains only partially explored by many aspects. The presence of "guest molecules" such as solubilized gas molecules (CO_2, H_2, CH_4, N_2, etc.) or any molecule which is present in addition to water and ionic species are expected to modify the thermodynamics and dynamics of the system [11–14]. In particular, oversolubility (i.e. large solubility increase in confinement with respect to its bulk counterpart), whose microscopic mechanisms have been unraveled only recently [15, 16], has been proposed in the literature (1) as the origin of striking observed catalytic kinetics [17, 18] and (2) as a mean to promote H_2 storage [19] or CO_2 capture [20, 21] in nanoporous materials. The so-called oversolubility effect can be described as follows [22, 23]; by reducing the liquid volume down to the nanometer scale (e.g. through

confinement in nanoporous materials or in nanofluidic devices), significant gas oversolubility – by a factor 10-100 in some cases – can be attained as compared to the bulk solubility predicted by Henry's law [24]. The underlying molecular origins for such gas uptakes in nanoconfined liquids have now been identified [15, 16]. It corresponds either to an adsorption-driven phenomenon that arises from the strong interaction between the gas and the pore surface or a confinement-induced enhanced solubility in which solubility is favored in the regions of low liquid density formed by the layering of the liquid. While a satisfying microscopic picture has been reached regarding the thermodynamics of oversolubility, its impact on diffusion in porous media has not been considered to date.

Here, we report on a combined experimental and theoretical investigation of gas oversolubility in nanoporous silicates and its impact on solvent and ionic diffusion in confinement. First, using statistical-mechanics molecular modeling (Monte Carlo and Molecular Dynamics), we show that CO_2, CH_4, H_2 are oversolubilized when confined in a realistic molecular model of a nanoporous aluminosilicate. Our results, which provide a microscopic picture of large gas dissolution rates observed in many available experimental data, further show that such oversolubility leads to drastically reduced diffusion compared to that observed in the absence of solubilized gases (we note that diffusion in confinement is already lower than the bulk diffusivity under the same thermodynamic conditions). Moreover, the amplitude of the dynamics slowdown becomes more pronounced as the strength of the gas intermolecular interactions at play increases (weak quadrupole, strong octopole, and strong quadrupole). Second, such dynamics slowdown is confirmed by using pulsed field gradient nuclear magnetic resonance experiments (PFG-NMR) to measure the diffusion coefficients of water confined in nanoporous silica and subjected to different pressures of gases. Our experimental findings, which probe the diffusion of confined water in the presence of different gases/pressures, are found to be qualitatively consistent with the picture emerging from the molecular simulation data. In particular, as expected, upon increasing the gas pressure, gas solubility increases and leads to further reduction in the water diffusivity in confinement.

Finally, the present paper also reports a simple physical model that allows rationalizing the oversolubility-induced slowdown observed both in the experimental and molecular simulation data. Despite the intrinsic complexity of diffusivity in such heterogeneous media, water and ion diffusivities are shown to follow a simple scaling law with the amount of solubilized gas (valid for all gases). To account for this scaling, we propose a molecular description in which the diffusivity decrease is explained by the increase in the confined fluid viscosity. Using the intimate link between diffusivity and viscosity, we invoke a simple free volume theory to explain the concomitant decrease in diffu-

sivity and increase in viscosity upon adding solubilized gases to the nanoconfined system. While further work is needed to unravel the details of such oversolubility-induced slowdown, the present work sheds light on confinement and transport of molecules in nanoconfined fluids in contact with gaseous atmospheres or with liquids containing solubilized gases. Understanding how oversolubility affects confining properties of porous materials is important to design efficient devices and processes for adsorption and catalytic engineering but also long-time transport in the context of pollutant migration (e.g. pollution and remediation in soils, underground radioactive waste storage [25, 26]).

Results

Gas oversolubility in nanoconfined water. While our fundamental study aims at elucidating the impact of oversolubility on the transport of nanoconfined species, we consider a system of high relevance to geological applications. In more detail, by treating the problem of water and ion diffusion in aluminosilicates (clay) in the presence of solubilized gases such as N_2, CH_4, and H_2, we cover a broad range of problems relevant to underground transport as involved in species migration and environmental pollution. However, in any case, despite the specificities of the system under study, the conclusions reported below are general so that they are expected to apply to most practical situations in other fields (as confirmed by the fact that the experiments reported in the present paper for a prototypical sample corroborate our main findings). Fig. 1(a) shows the molecular model used to investigate gas solubility in hydrated clay. The clay considered in this work is Na-montmorillonite which is obtained from isomorphous (Si/Al and Mg/Al) substitutions in both the tetrahedral and octahedral sheets $[Na_{0.75}(Si_{7.75}Al_{0.25})(Al_{3.5}Mg_{0.5})O_{20}(OH)_4]$. The simulation box is made up of two rigid, parallel sheets (each of them containing eight unit cells). Two different interlayer spacings d are considered, 12.5 Å and 15.5 Å, which correspond to the experimental spacings in the monolayer and bilayer hydrated states for sodium montmorillonite (see Methods section and Supplementary Section 1).

Clay hydration in the monolayer and bilayer states was first simulated using Grand Canonical Monte Carlo simulations at different relative humidity RH. Fig. 1(b) shows the amount of water in Na-montmorillonite as a function of RH (defined as the water relative vapor pressure P/P_0 where P_0 is the bulk saturating vapor pressure). For a given water pressure, we impose the interlayer spacing observed in experiments [27], $d = 12.5$ Å for $P < 0.75P_0$ and $d = 15.5$ Å for $P > 0.75P_0$. In agreement with experimental data, as will be discussed below, these two interlayer spacings

accommodate one and two water layers, respectively. The corresponding adsorbed amounts are $n_a \sim 60 - 80$ mg of water per g of clay and $n_a \sim 160 - 180$ mg of water per g of clay, respectively. As shown in Fig. 1(b), the simulated adsorbed amount at a given pressure were found to be in reasonable agreement with available experimental data [28, 29]. Hereafter, to consider different thermodynamic conditions relevant to underground conditions, we consider the following hydration states at a temperature $T = 363$ K: RH = 55% (monolayer state) and RH = 95% (bilayer state).

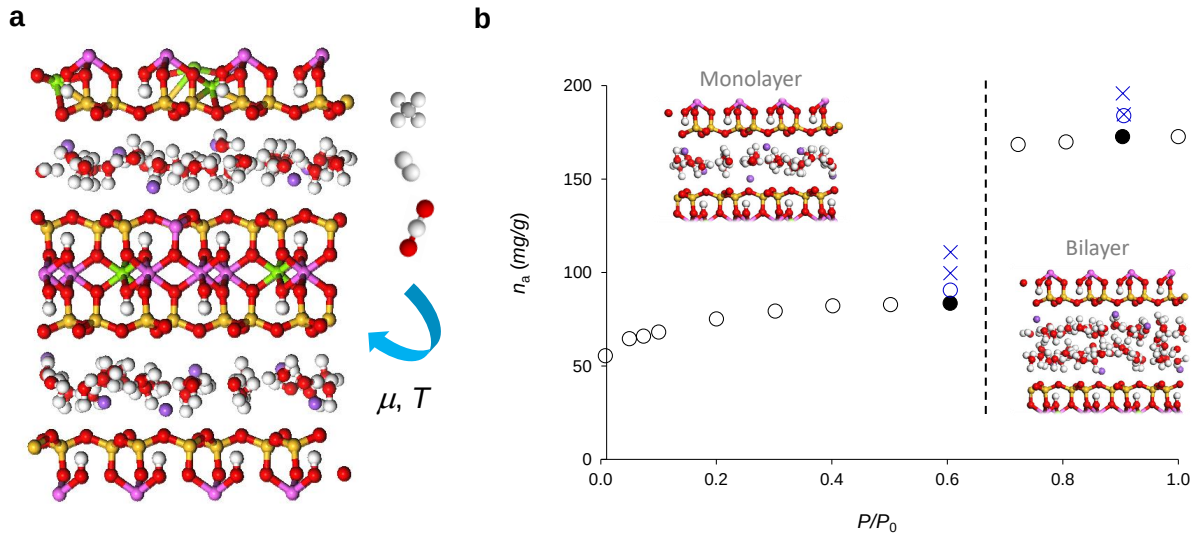

FIG. 1: **Water adsorption and swelling in a clay molecular model.** **a**, Molecular model used to investigate gas oversolubility in a hydrated clay of the type Na-montmorillonite. Different gases (CO_2, CH_4, and H_2) are adsorbed in hydrated clay at a temperature $T = 363$ K and different pressures P. Here, the clay is at low relative humidity where water in the clay interlayer space forms a monolayer. The color code for the hydrated clay is yellow (Si), red (O), white (H), pink (Al), purple (Na), and green (Mg). **b**, Simulated water adsorption isotherm at $T = 363$ K in Na-montmorillonite (black circles). The x-axis corresponds to the water vapor pressure (i.e. relative humidity RH) while the y-axis is the amount of water adsorbed in the interlayer spacing expressed in mg of water per g of clay. The sharp increase corresponds to swelling from the interlayer spacing $d = 12.5$ Å(water monolayer) to $d = 15.5$ Å (water bilayer). The molecular simulation results at $T = 298$ K (blue circles) for the monolayer and bilayer states are also shown and compared with the experimental data (blue crosses) from Refs. [28, 29].

Gas solubility in the two hydrated clay conditions was then investigated using Grand Canonical Monte Carlo simulations by imposing a chemical potential corresponding to CO_2, H_2 or CH_4 pressures in the range 0-120 bars. Fig. 2 shows the simulated CO_2, CH_4 and H_2 solubility curve in hydrated clay at $T = 363$ K for pressures up to $P = 120$ bar. The data for both hydration states (monolayer and bilayer) are shown together with the solubility curve for bulk water. The solubility

S is given as the ratio of the number of solubilized molecules to the number of water molecules. For each gas, the solubility in the hydrated clay is larger than the bulk solubility over the whole pressure range. Moreover, for a given pressure, the gas solubility is larger for the monolayer state than for the bilayer state. As explained earlier, such enhanced solubility, which corresponds to a striking increase of gas solubility in confined solvents with respect to the values predicted by Henry's law, is referred to as "oversolubility" in the literature. For both hydrated clays, CO_2 exhibits greater solubility than CH_4 and H_2 due to its stronger interaction with both the host solid and water. In addition, the solubility of CH_4 is greater than that of H_2 over the entire pressure range because of its higher polarizability. We find that the H_2 and CH_4 solubilities follow Henry's law as the gas uptake increases linearly with the pressure. In contrast, Henry's law breaks down in the case of CO_2 for the reasons explained in the next paragraph.

Different possible physical origins of oversolubility were previously identified [15]. Depending on the gas and solvent considered, two microscopic mechanisms at the heart of oversolubility were highlighted. On the one hand, gas uptake can be an adsorption-driven phenomenon which occurs because of favorable adsorption at the solvent/solid interface. On the other hand, gas uptake can be a confinement-induced enhanced solubility in which solubility is favored in the regions of low solvent density formed by the layering of solvent molecules. To unravel the nature of oversolubility for CO_2, CH_4 and H_2 in hydrated clay, we determined the density profiles for the different species within the interlayer spacing of hydrated clay. Fig. 3(a) shows the density profiles for water, sodium cations, CO_2, CH_4, and H_2 as a function of the distance z with respect to the interlayer center. These data were obtained for a gas pressure of 60 bar with the interlayer spacings d = 12.5 Å and d = 15.5 Å. Note that the density profiles for water and sodium in the presence of solubilized gases are not shown in Fig. 3(a) as very similar data to those without solubilized gases were obtained. This is due to the fact that the distribution of water and counterions in the clay interlayer spacing is governed by strong electrostatic forces which are not affected by the presence of weakly interacting guest species such as CO_2, CH_4, and H_2. As expected, the density profiles for water display one and two well-defined density layers in the monolayer and bilayer hydration states, respectively. The three gases form the same number of well-defined layers which are located at similar positions as those for water. The carbon dioxide molecules are preferentially oriented parallel to the clay surface, as revealed by the fact that the C and O atoms of the CO_2 molecules are located at a very similar z-position (for the bilayer state, the atoms are not at the exact same position but the orientation remains overall very close to parallel orientation). These observations are consistent with those reported by Botan et al. for CO_2 adsorbed in hydrated clay

[30]. The sodium cations form two symmetrical layers for the monolayer state and three layers for the bilayer state. This result suggests that all the cations for the monolayer state are located close to the surface in the vicinity of the charge defects that they counterbalance. For the bilayer state, the peak in the middle of the interlayer spacing suggests that some of the ions are not immobilized close to the clay layer.

The results above suggest that gas oversolubility in clay pertains to a combined effect of adsorption-driven oversolubility and bulk-like enhanced oversolubility. On the one hand, in adsorption-driven solubility, enhanced solubility occurs at the pore surface due to the strong interaction between the solubilized gas and the surface. On the other hand, in bulk-like enhanced solubility, oversolubility occurs in regions of low solvent (water) density which arise from density oscillations close to the pore surface. In the case of CO_2, CH_4 and H_2 solubilized in water confined in Na-montmorillonite, the structural data above suggest that, owing to the heterogeneity of the clay interlayer surface, both water and the gas molecules are adsorbed at the pore surface. In fact, while water is adsorbed close to the Na^+ ions and the O atoms of the surface through strong electrostatic/dispersion interactions, the gas molecules remain adsorbed in the vicinity of the surface but in sites where water is not present. Analysis of the radial distribution functions $g(r)$ between the different species in the monolayer and bilayer states further supports this interpretation (see Supplementary Figs. 1 and 2 and the related Supplementary Section 2). The fact that oversolubility in water confined in clay corresponds to a mixture of (1) bulk-like solubility within the water density minima and (2) adsorption at the clay surface is an unprecedented result (all previously reported oversolubility effects corresponds to one of these phenomena). This result is due to the heterogeneity of the clay surface; while water is adsorbed in locations where it solvates the Na^+ cations, gas molecules become solubilized in between the adsorbed water molecules. As a result, the density peaks corresponding to water and gas adsorbed layers appear at the same position.

Impact on water and ion diffusion. The dynamical properties of the hydrated nanoporous clay in the presence of solubilized gas molecules was investigated by probing the dynamics of water and cations when CO_2, CH_4 or H_2 is adsorbed. In particular, the effect of oversolubility on diffusion in confining clay was assessed using Molecular Dynamics by probing the self-diffusivity for each species in the monolayer and bilayer states (see Methods section). Fig. 3(b) shows the average mean square displacement $\langle \Delta r^2(t) \rangle$ as a function of time t for water molecules and sodium cations in the bilayer state in the absence and in the presence of the solubilized gases (Supplementary Fig. 3 shows the same results for the monolayer state). These data show that both water and sodium reaches the Fickian regime where $\langle \Delta r^2(t) \rangle \sim t$ after a few ps. The self-diffusion coefficients D_s for

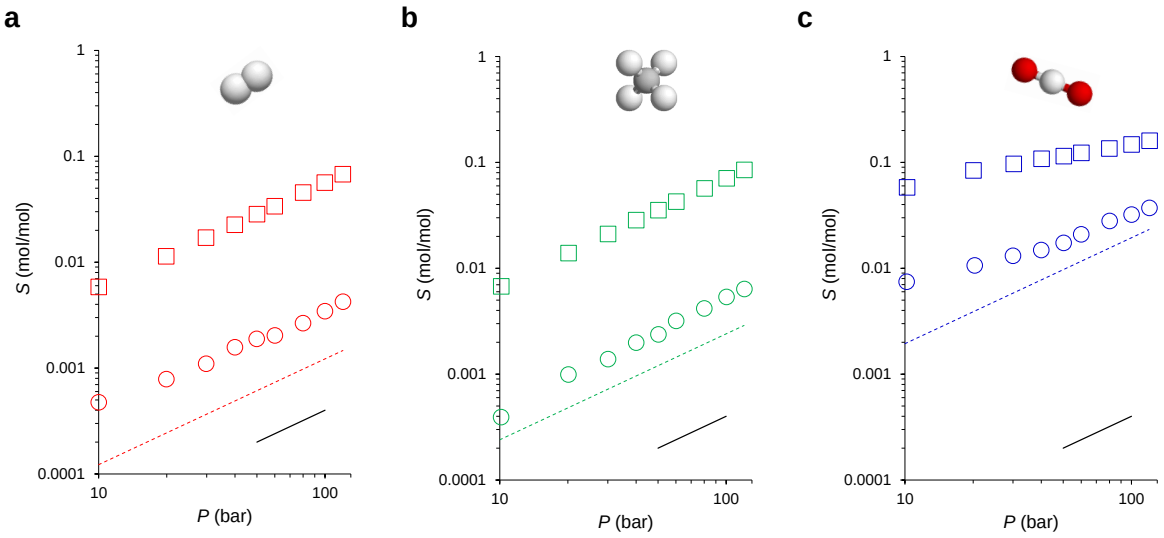

FIG. 2: **Gas oversolubility in hydrated nanoporous clay.** Simulated gas solubility S at $T = 363$ K in a hydrated clay as a function of the gas pressure P: (**a**) H_2, (**b**) CH_4, and (**c**) CO_2. The circles and squares are for hydrated clays with a water bilayer and a water monolayer, respectively. The dashed lines show the bulk solubility while the black solid lines indicate a power law $S \sim P$ as expected in Henry's regime (note the use of a log-log scale).

water and sodium were calculated from the slope of the mean square displacements in the Fickian regime:

$$D_s = \frac{1}{6} \lim_{t\to\infty} \frac{\mathrm{d}\langle \Delta r^2(t)\rangle}{\mathrm{d}t} \tag{1}$$

For both hydration states, the magnitude of the self-diffusivities for water and sodium cations in the clay subjected to gas oversolubility follows the following order: no gas $>$ H_2 $>$ CH_4 $>$ CO_2. Focusing on the data obtained for water in the presence of solubilized gases, the data for hydrogen shows the largest water self-diffusivity with $D_s = 0.40 \times 10^{-9}$ m^2.s^{-1} and 4.62×10^{-9} m^2.s^{-1} in the monolayer and bilayer states ($D_s = 0.15 \times 10^{-9}$ m^2.s^{-1} and 3.56×10^{-9} m^2.s^{-1} for the sodium cations). In contrast, CO_2 exhibits the lowest water self-diffusivity $D_s = 0.17 \times 10^{-9}$ m^2.s^{-1} and 3.47×10^{-9} m^2.s^{-1} in the monolayer and bilayer states ($D_s = 0.08 \times 10^{-9}$ m^2.s^{-1} and 1.48×10^{-9} m^2.s^{-1} for the sodium cations). Overall, the results above suggest that the presence of solubilized gases hinder water and ion diffusion in clay interlayer spacing by about 10% to 66% depending on the specific thermodynamic conditions under consideration.

Viscosity and free volume theory. With the aim to propose a molecular model for diffusion in confined geometries in the presence of solubilized gases, we compare in Fig. 4(b) the self-diffusivites

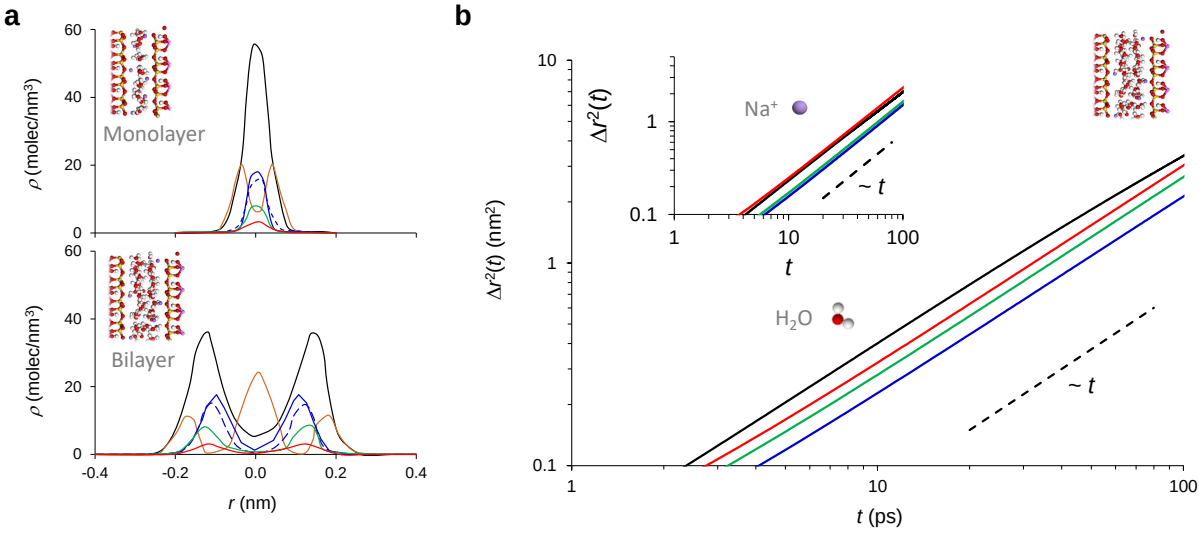

FIG. 3: **Structure and dynamics of water and sodium cations in the clay nanoporosity**. **a**, Density profiles for the C atom of the CO_2 (blue), O atom of the CO_2 (dash line-blue), CH_4 (green), H_2 (red), Na^+ (orange) and O atom of water (black) in the monolayer (top) and bilayer (bottom) hydration states of Na-montmorillonite clay. For the sake of clarity, the density of Na^+, $C(CO_2)$, $O(CO_2)$, CH_4 and H_2 was multiplied by a factor of 2 for the monolayer state and by a factor of 3 for the bilayer state. **b**, Simulated mean square displacements $\Delta r^2(t)$ as a function of time t for water at $T = 363$ K in hydrated clay (bilayer state) subjected to gas oversolubility. The black line is for water when no gas is solubilized in the clay interlayer spacing while the red, blue and green lines are for water when H_2, CO_2 and CH_4 are solubilized in the clay interlayer spacing. The black dashed line indicates the power law $\Delta r^2 \sim t$ expected in the Fickian regime. The insert shows the same results for the cation Na^+.

of water molecules and sodium cations. For a given hydration state, the decrease in self-diffusivity for the two species are found to be proportional to each other. This result suggests that the self-diffusion decrease for both species can be related to a change in the viscosity of the confined solvent (water). In more detail, by invoking the Stokes-Einstein equation which relates the water viscosity η to the water/ion diffusivities, we write:

$$D_s^i = \frac{k_B T}{6\pi\eta a_i} \tag{2}$$

where i refers to the sodium cation or water molecule and a_i corresponds to the kinetic diameter of the diffusing species. In agreement with the data in Fig. 4(b), we predict that the self-diffusivities $D_s(\mathrm{Na})$ and $D_s(H_2O)$ are related through a proportionality factor given by $a_{\mathrm{Na}}/a_{\mathrm{H2O}}$. Quantitatively, we find that $a_{\mathrm{H2O}} \sim 0.44 a_{\mathrm{Na}}$ and $a_{\mathrm{H2O}} \sim 0.68 a_{\mathrm{Na}}$ for the monolayer and bilayer states, respectively. These values are roughly consistent with the data obtained for Na and water diffusion

in bulk NaCl aqueous electrolytes [31]). However, strikingly, the ratio $a_{\mathrm{Na}}/a_{\mathrm{H2O}}$ obtained for the bulk electrolyte ($a_{\mathrm{H2O}} \sim 0.40 - 0.41 a_{\mathrm{Na}}$) is closer to the value obtained for the monolayer state than for the monolayer state. Such a result, which seems counterintuitive at first, since water in the bilayer state is less confined than in the monolayer state can be rationalized as follows. Close inspection of the data in Fig. 3(a) shows that the density profile for the sodium cations in the monolayer state overlaps more with the water density profile than in the bilayer state. In contrast, in the bilayer state, while some cations are localized near the surface where they are hydrated, a non-negligible share of the cations are located in the pore center without significantly overlapping with the two adsorbed water layers. As a result, despite more pronounced confinement effects in the monolayer state, the sodium cations experience in this local environment a friction force (impact of water viscosity) that is closer to its bulk counterpart than in the bilayer state.

While the Stokes-Einstein relation allows rationalizing the consistent decrease in the self-diffusivity of water and the sodium cations, it does not explain the change in the viscosity η observed upon gas oversolubility. Such an increase in the water viscosity or, equivalently, decrease in the water diffusivity can be described using a free volume theory. This model, which was initially developed for diffusion in bulk liquids including complex systems such as polymers [32], has been successfully used for alkane transport in nanoporous materials [33, 34]. In this theory, one writes that the self-diffusivity $D_s(N)$ for N water molecules having a molecular volume v is related to the accessible free volume $V_f(N)$ in the liquid:

$$D_s(N) = D_s(0) \exp\left[- \frac{\alpha N v}{V_f(N)} \right] \tag{3}$$

where $D_s(0)$ is the self-diffusivity of an isolated molecule (infinite dilution) and $V_f(N)$ is the free volume accessible to the N molecules. α is an overlap coefficient, considered as a fitting parameter, that takes into account the fact that free cavities for different molecules overlap (in other words, different molecules cannot diffuse within the same cavities so that α can be seen as a steric repulsion parameter). In the context of the present study, one has to take into account that for a given hydration state the free volume inside the clay interlayer spacing depends on the number of water molecules N and the number of gas molecules n_g, i.e. $V_f = V_f(N, n_g)$. With these elements, Eq. (3) can be recast as:

$$D_s(N, n_g) = D_s(N, 0) \exp\left[- \alpha N v \left(\frac{1}{V_f(N, n_g)} - \frac{1}{V_f(N, 0)} \right) \right] \tag{4}$$

where N is the number of water molecules in the system (in practice, it was found that gas oversolubility leads to a slight decrease in the number of water molecules in the clay but this

difference was neglected here as it was found to be small). To test the validity of this simple model, we used $v = 1/\rho_w \sim 0.031$ nm^3 (ρ_w is the number density of water of the liquid phase at the temperature considered in our simulations). The change in free volume V_f upon solubilizing n_g gas molecules was estimated as $V_f(N, n_g) = V_f(N, 0) - \alpha n_g v_g$ where v_g is the volume of a gas molecule. We used $v_g = 4/3\pi(\sigma_g/2)^3$ where σ_g is the gas kinetic diameter ($\sigma_g = 0.28$ nm, 0.33 nm, and 0.38 nm for H_2, CO_2 and CH_4, respectively). Within these approximations, we can express Eq. (4) as:

$$\ln \frac{D_s(N, n_g)}{D_s(N, 0)} = -\beta N v \left[\frac{1}{1 - \beta n_g v_g} - 1 \right] \tag{5}$$

where $\beta = \alpha / V_f(N, 0)$ is the only fitting parameter in our model. To ensure that the description proposed here and the underlying free volume model are physically accurate, we impose in our fit that $[V_f(N, 0)/\alpha]_{\text{bilayer}} = 2[V_f(N, 0)/\alpha]_{\text{monolayer}}$ (i.e. the free volume in the bilayer state is twice the free volume in the monolayer state). As can be seen in the inset of Fig. 3(b), for both the monolayer and bilayer states, this simple free volume model captures the change in the water self-diffusivity upon adding solubilized gases to the confined system. In particular, by comparing the data for the different gases, the model accurately describes the fact that the self-diffusivity decrease is more pronounced as the gas interactions increase ($H_2 > CH_4 > CO_2$). Finally, it is interesting to consider the limit of low solubilization by taking the limit $\beta n_g v_g << 1$. Under such conditions, we can derive a linearized version of Eq. (5) which writes: $D_s(N, n_g) - D_s(N, 0) \sim n_g v_g$. As can be seen in Supplementary Fig. S5, in agreement with this simple scaling, it is observed that $D_s(N, n_g) \sim n_g v_g$ for the different gases and hydration states. From a practical viewpoint, such a simple scaling provides a means to estimate the expected decrease in diffusivity when oversolubility occurs.

Experiments on confined water diffusion. As a final step, with the goal to validate the oversolubility-induced slowing down in pores observed in our molecular simulations, we conducted PFG-NMR experiments at room temperature on water diffusion in hydrated silica. Clay samples are difficult to handle in NMR experiments as they contain metal species which can cause enhanced relaxation. To circumvent this technical difficulty, an ordered nanoporous silica displaying cylindrical pores with a diameter of a few nm was used as a proxy materials (See Methods section). More specific interactions are expected in the case of water diffusion in clay but nanoporous silica is sufficient to provide an experimental proof of the oversolubility-induced slowing down observed in our atom-scale simulations. In more detail, for the fully hydrated nanoporous silica, we investigated the effect of gas solubility on water diffusivity for the three following gases: CO_2, CH_4,

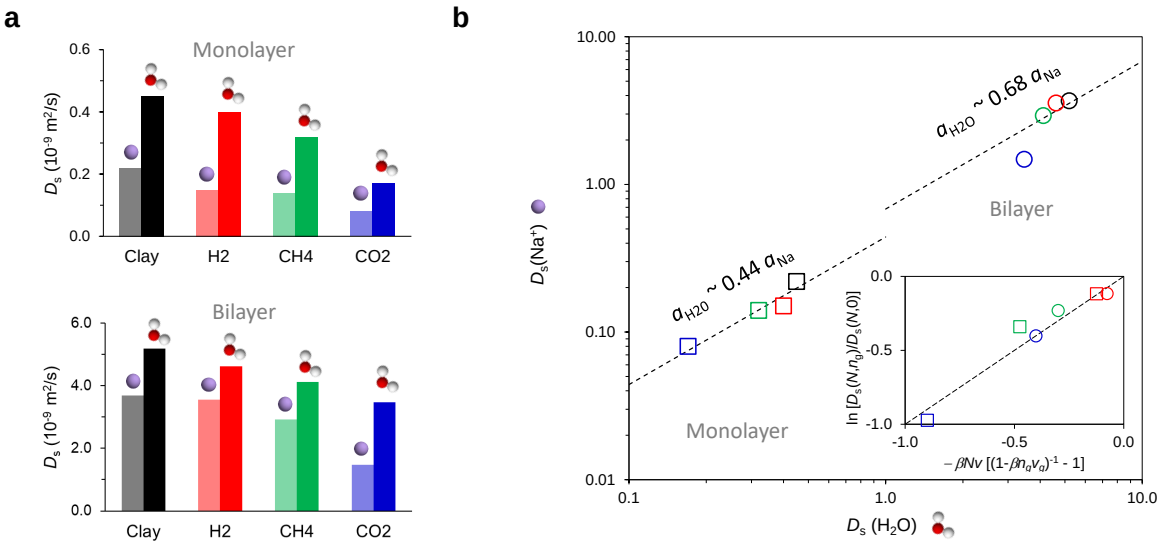

FIG. 4: **Dynamical slowdown in nanoconfined phases subjected to oversolubility. a**, Self-diffusivity for Na^+ and water confined in montorillonite clay at different relative humidity: (top) monolayer state, (bottom) bilayer state. The data show the diffusivities for water and sodium cations in clay without any solubilized gas (black) or with solubilized H_2 (red), CH_4 (green) and CO_2 (blue). Note the y-axes used for the two series which is one order of magnitude smaller for the monolayer state than for the bilayer state. Self-diffusivity for sodium cations Na^+ as a function of the self-diffusivity for water in clay at different relative humidity conditions (monolayer and bilayer states). The black data correspond to clay without any solubilized gas while the red, green, and blue data correspond to the same system in the presence of oversolubilized H_2, CH_4 and CO_2, respectively. As described in the main text, the dashed lines indicate that $D_s(Na^+)$ and $D_s(H_2O)$ are proportional with different proportionality factors in the monolayer and bilayer states. The inset shows the validity of the free volume theory to rationalize the change in the self-diffusivity of the confined fluid (water) when adding oversolubilized gases in the hydrated clay: the circles and squares correspond to the data for the bilayer and monolayer states, respectively.

and N_2. PFG-NMR probes the diffusivity of hydrogenated compounds by encoding their ^{1}H spins. We could not detect ^{1}H NMR signals from dissolved H_2 gas due to their low concentration, hence, the PFG NMR experiments are only able to measure the diffusion constant for water molecules. For each gas, the hydrated silica sample was set in contact with a reservoir of gas molecules at a pressure of 1 bar. In the case of CO_2, we also determined the effect of the gas pressure by considering a gas reservoir at a pressure of 3 bar.

Fig. 5 shows the experimental self-diffusivity D_s at room temperature for confined water subjected to gas oversolubility at a pressure of 1 bar. These data, which are typical of data obtained using PFG-NMR, are plotted as a function of the time scale probed $[D_s(0)t]^{1/2}$ where

$D_s(0) \sim 1.9 \times 10^{-9}$ m^2.s^{-1} is the self-diffusivity of bulk liquid water under similar thermodynamic conditions. The long-time diffusivity $D_s(\infty)$ was obtained by fitting the data shown in Fig. 5 using $D_s(t) - D_s(\infty) \sim D_s(0)/t$ for large t. The amount of solubilized gas is not known in such experiments but our diffusion measurements provide clear evidence that gas solubility leads to a strong decrease in the self-diffusivity of confined water. We note that typical diffusivity reductions observed in the diffusion experiments in the presence of solubilized gases are consistent with the molecular simulation data reported above. This result is further validated by our diffusion experiments performed for confined water set in contact with different CO_2 pressures. Indeed, upon increasing the CO_2 pressure from 1 to 3 bar, we observe in Fig. 5 further reduction in the self-diffusivity of water confined in nanoporous silica.

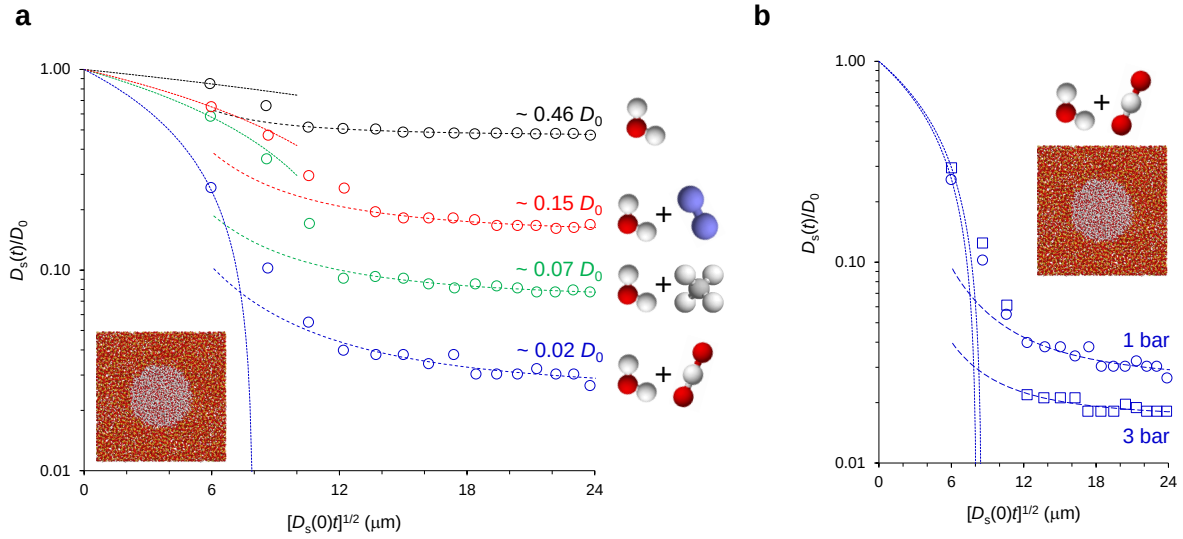

FIG. 5: **NMR Experiments on confined water diffusion.** **a**, Experimental self-diffusivity $D_s(t)$ at room temperature as observed using pulsed field gradient nuclear magnetic resonance for water confined in silica cylindrical nanopores subjected to gas oversolubility at a pressure of 1 bar: (red circles) N_2, (green circles) CH_4, and (blue circles) CO_2. The black circles are for confined water in the absence of solubilized gases. For the sake of illustration, the inset shows a molecular configuration showing water nanoconfined in a cylindrical silica nanopore. The experimental data are plotted as a function of the time scale probed (expressed as $[D_s(0)t]^{1/2}$ where $D_s(0)$ is the self-diffusivity observed at very short time scale). The self-diffusivity $D_s(t)$ is normalized to $D_s(0)$. For each data set, the dashed line shows a fit of the data in the long-time scale i.e. $D_s(t) - D_s(\infty) \sim D_s(0)/t$ while the dotted line shows a fit of the data in the short-time scale i.e. $D_s(0) - D_s(t) \sim [D_s(0)t]^{1/2}$. **b**, Same as in (a) but for the diffusivity of confined water in the presence of solubilized CO_2 at different pressures: $P = 1$ bar (circles) and $P = 3$ bars (squares).

Discussion

Using a combined molecular simulation and experimental approach, we demonstrated that oversolubility strongly affects the dynamics of molecular and ionic species confined in nanoporous materials. By invoking a simple statistical physics model (free volume theory), we proposed a microscopic description to account for the impact of the oversolubilized gas on the viscosity and the self-diffusivity of the nanoconfined species. This simple formalism offers a valuable framework to predict how oversolubility effects affect confinement and transport properties of hybrid systems, i.e. porous materials filled with a liquid (solvent). Once integrated into a bottom-up model of fluid transport in multiscale porous materials, the comprehensive and unifying picture of such oversolubility effects can be used to develop and optimize new adsorbents and processes relevant to adsorption/separation, catalysis/chemical reactions, energy storage, etc. Beyond immediate implications, the results reported here about the impact of oversolubility on transport in nanoporous materials also raises new challenging fundamental questions. In particular, the work proposed here is a step forward in taking into account the response of nanoporous materials – in terms of confinement and transport properties – to chemical stimuli as induced for instance by the presence of other interacting species (gases, pollutants, solutes, etc.).

The effects of oversolubility on transport in nanoconfinement is also relevant to major issues such as the modeling of transfer mechanisms in porous materials in the presence of specific interactions between nanoporous materials and confined liquids/guest molecules (including waste and pollutants). In addition to fundamental and practical questions relevant to chemistry, physical chemistry, and chemical engineering, a better understanding of transport in nanoporous materials subjected to such oversolubility effects is also relevant to many other practical fields such as civil engineering and soil science. Among important questions related to the latter field, the durability of anthropic materials (adsorption and transport of corrosive species in the porosity of concrete is responsible in part for their deterioration) and pollutant transport in soils and underground media (dispersion of waste and pollutants over time) are expected to be strongly affected by potential oversolubility effects and related transport aspects.

Methods

A. Computational details

Molecular models. The size of the simulation box for the two hydrated states are: 20.64 Å× 17.94 Å× 25.74 Å and 20.64 Å× 17.94 Å× 31.7 Å, respectively, with $\alpha = 91.18°$, $\beta = 100.46°$, and $\gamma = 89.64°$. Periodic boundary conditions were used in the x, y, and z directions in order to avoid finite size effects. The partial charges and Lennard-Jones parameters of the framework atoms, which are taken from the CLAYFF force field [35]. The single point charge (SPC) model by Berendsen et al. [36] is used for water as it quantitatively reproduces the bulk saturating vapor pressure of water. Supplementary discussion 1 presents in detail the molecular models and force fields used to describe the CO_2, CH_4 and H_2 molecules. The partial electrostatic charges and Lennard-Jones parameters of the clay and fluid atoms are shown in Supplementary Table 1. The LJ cross interaction parameters (σ_{ij}, ε_{ij}) between unlike sites are calculated using the Lorentz-Berthelot combining rules.

Grand Canonical Monte Carlo. Gas adsorption in the hydrated clay is investigated using Grand Canonical Monte Carlo (GCMC) simulations. The simulation methodology follows the procedure proposed by Ho et al.[21] for different porous materials. The hydrated clay is prepared by filling its interlayer spacing with water molecules. In order to simulate in a realistic fashion water loading in clay, GCMC simulations are performed by adjusting the chemical potential μ of the water external reservoir. We then simulate gas adsorption in the hydrated clays by imposing a chemical potential corresponding to a given pressure of CO_2, H_2 or CH_4. The absolute gas adsorption isotherms in the hydrated clays are calculated as the ensemble average number $\langle N \rangle$ of adsorbed molecules as a function of the pressure at constant temperature (the pressure P is readily obtained from the chemical potential μ using the ideal gas law). In the course of the molecular simulations, the framework of the clay is kept rigid. Periodic boundary conditions are applied in all three directions. Our simulations are performed for different gas pressures P in the range 0-120 bars.

Molecular Dynamics. Molecular Dynamics (MD) simulations are performed using starting configurations obtained from the Monte Carlo simulations described above. Such MD simulations are carried out in the Canonical ensemble (constant NVT where N, V and T are the number of molecules, the volume and temperature of the system) with the DLPOLY code [37]. The integration time step is 1 fs and the temperature is fixed using a Nosé-Hoover with a relaxation time of 100

fs. All the simulations are first performed for a total of 10 ps to reach equilibrium configurations before statistical averages are collected. Once equilibrium is reached, configurations are sampled every 0.5 ps and the production runs are 3 ns long.

B. Experimental details

Fluids and materials. Deionized water (resistivity > 18 Ω/cm) was used as solvent. Nitrogen, carbon dioxide and methane gases (purity $> 99.99\%$) were obtained from Air Liquide (France). The confining mesoporous solid was a mesostructured MCM-41 with the following main textural properties: skeletal density 2.3 g/cm^3, BET specific surface 1065 m^2/g, pore volume 1.086 cm^3/g, mean pore size 3-4 nm [19]. These features were measured on our premises by He picnometry (skeletal density) and N_2 adsorption at 77.4 K using a Micromeritics ASAP 2020 apparatus (BET specific surface, mesopore volume and mean pore size). The MCM 41 (Si/Al $\rightarrow \infty$) was synthesized using the following protocol. Hexadecyltrimethylammonium-p-toluene-sulfonate (CTATos, 6.4 g) was dissolved in deionized water (462 mL) at 333 K. A silicate solution (160 mL) prepared by dissolution of NaOH (32.0 g) and Ludox (187 mL) in 800 L deionized water was added dropwise under mild stirring. After 2h stirring, the solution was subjected to hydrothermal synthesis in a Teflon-lined autoclave at 403 K for 20 h. After the synthesis, the solid was filtered, washed with deionized water (3x100 mL) and dried overnight at 353 K. The surfactant was then extracted using HCl (1 M) in EtOH (96%) at 313 K for 80 min. The sample was finally calcined at 823 K for 6 h under air flow.

Sample preparation. The hybrid adsorbent consisting of the MCM-41 filled with water was prepared by partially filling the pore volume of the confining mesoporous solid with water *via* wet impregnation using the experimental procedure presented in a previous study [19]. After impregnation, the impregnated MCM-41 was placed into a 5 mm NMR tube that was equipped with a quick pressure valve (Wilmad, Inc.). The adapter on the NMR tube enabled the impregnated sample to be contacted with a gas atmosphere at the indicated pressure. The samples were first evacuated at a pressure of 0.1 bar to remove adsorbed air, then the atmosphere was switched to that of the desired pressure. The sample was allowed to rest for *ca.* 15 minutes at the desired pressure to equilibrate the concentration of dissolved gases. The valve at the NMR tube was then closed and the pressurized sample was placed into the NMR spectrometer. The following gases and conditions were considered at ambient temperature: N_2 and CH_4 at a pressure of 1 bar and CO_2 at pressures of 1 bar and 3 bar.

Pulsed-Field Gradient Nuclear Magnetic Resonance. Proton NMR data were collected at room temperature (25°C) using a Bruker Avance III 600 MHz spectrometer, with a 5 mm triple-resonance cryoprobe equipped with Z gradients. Pulsed field gradient stimulated echo (PFG-STE) diffusion experiments were implemented to measure the diffusion coefficient. The successful setup of the PFG-STE pulse sequence and calibrations of the gradients were separately checked by measuring the diffusion constants of acetonitrile and methanol [38, 39]. Sine shaped gradients of 4 ms duration were incremented in 15 steps with 16 scans each. The gradient strength was increased from 0 to 24 G/cm. The proton 90° pulse width was of 8 μs and the length of the spoil gradient was 1 ms. A series of PFG NMR experiments was performed with diffusion times varying from 20 ms to 300 ms for each set of samples.

Data availability

The data generated and/or analyzed in the present study are available from the corresponding author upon request. All MD simulations were performed using the software DLPOLY (Version 3).

[1] M. Thommes, K. Kaneko, A. V. Neimark, J. P. Olivier, F. Rodriguez-Reinoso, J. Rouquerol, and K. S. Sing, Pure and Applied Chemistry **87** (2015), URL https://amu.hal.science/hal-01416682.

[2] L. Bocquet and E. Charlaix, Chem. Soc. Rev. **39**, 1073 (2010).

[3] B. Smit and T. Maesen, Chem. Rev. **108**, 4125 (2008).

[4] B. Coasne, New J. Chem. **40**, 4078 (2016).

[5] J. Kärger, D. M. Ruthven, and D. N. Theodorou, *Diffusion in Nanoporous Materials* (John Wiley & Sons, 2012), ISBN 978-3-527-65129-0.

[6] K. Hahn and J. Kärger, The Journal of Physical Chemistry B **102**, 5766–5771 (1998), ISSN 1520-5207, URL http://dx.doi.org/10.1021/jp981039h.

[7] C. Bousige, P. Levitz, and B. Coasne, Nature Communications **12**, 1043 (2021), URL https://hal.science/hal-03141574.

[8] T. Lee, L. Bocquet, and B. Coasne, Nature Communications **7** (2016), ISSN 2041-1723, URL http://dx.doi.org/10.1038/ncomms11890.

[9] F. Schüth, K. Sing, , and T. Weitkamp, *Handbook of porous solids* (Wiley-VCH, 2002).

[10] P. V. D. Voort, K. Leus, and E. D. Canck, *Introduction to Porous Materials* (Wiley, 2019).

[11] T. Bui, A. Phan, D. R. Cole, and A. Striolo, The Journal of Physical Chemistry C **121**, 15675–15686 (2017), ISSN 1932-7455, URL http://dx.doi.org/10.1021/acs.jpcc.7b02713.

[12] G. Camisasca, A. Tinti, and A. Giacomello, The Journal of Physical Chemistry Letters **11**, 9171–9177 (2020), ISSN 1948-7185, URL http://dx.doi.org/10.1021/acs.jpclett.0c02600.

[13] A. G. Ilgen, K. Leung, L. J. Criscenti, and J. A. Greathouse, Annual Review of Physical Chemistry **74**, 169–191 (2023), ISSN 1545-1593, URL http://dx.doi.org/10.1146/annurev-physchem-083022-030802.

[14] J. Lee and N. R. Aluru, The Journal of Physical Chemistry C **115**, 17495–17502 (2011), ISSN 1932-7455, URL http://dx.doi.org/10.1021/jp205260j.

[15] L. N. Ho, S. Clauzier, Y. Schuurman, D. Farrusseng, and B. Coasne, The Journal of Physical Chemistry Letters **4**, 2274–2278 (2013), ISSN 1948-7185, URL http://dx.doi.org/10.1021/jz401143x.

[16] B. Coasne and D. Farrusseng, Microporous and Mesoporous Materials **288**, 109561 (2019), ISSN 1387-1811, URL http://dx.doi.org/10.1016/j.micromeso.2019.109561.

[17] J. Peureux, M. Torres, H. Mozzanega, A. Giroir-Fendler, and J.-A. Dalmon, Catalysis Today **25**, 409–415 (1995), ISSN 0920-5861, URL http://dx.doi.org/10.1016/0920-5861(95)00128-3.

[18] V. Rakotovao, R. Ammar, S. Miachon, and M. Pera-Titus, Chemical Physics Letters **485**, 299–303 (2010), ISSN 0009-2614, URL http://dx.doi.org/10.1016/j.cplett.2009.12.038.

[19] S. Clauzier, L. N. Ho, M. Pera-Titus, B. Coasne, and D. Farrusseng, Journal of the American Chemical Society **134**, 17369–17371 (2012), ISSN 1520-5126, URL http://dx.doi.org/10.1021/ja308157a.

[20] C. Song, Catalysis Today **115**, 2–32 (2006), ISSN 0920-5861, URL http://dx.doi.org/10.1016/j.cattod.2006.02.029.

[21] L. N. Ho, Y. Schuurman, D. Farrusseng, and B. Coasne, The Journal of Physical Chemistry C **119**, 21547–21554 (2015), ISSN 1932-7455, URL http://dx.doi.org/10.1021/acs.jpcc.5b06660.

[22] A. Luzar and D. Bratko, The Journal of Physical Chemistry B **109**, 22545–22552 (2005), ISSN 1520-5207, URL http://dx.doi.org/10.1021/jp054545x.

[23] D. Bratko and A. Luzar, Langmuir **24**, 1247–1253 (2007), ISSN 1520-5827, URL http://dx.doi.org/10.1021/la702328w.

[24] A. L. Myers, AIChE Journal **16**, 157–157 (1970), ISSN 1547-5905, URL http://dx.doi.org/10.1002/aic.690160103.

[25] G. Gadikota, B. Dazas, G. Rother, M. C. Cheshire, and I. C. Bourg, The Journal of Physical Chemistry C **121**, 26539–26550 (2017), ISSN 1932-7455, URL http://dx.doi.org/10.1021/acs.jpcc.7b09768.

[26] N. Stolte, R. Hou, and D. Pan, Nature Communications **13** (2022), ISSN 2041-1723, URL http://dx.doi.org/10.1038/s41467-022-33696-w.

[27] S. Morodome and K. Kawamura, Clays and Clay Minerals **57**, 150–160 (2009), ISSN 1552-8367, URL http://dx.doi.org/10.1346/CCMN.2009.0570202.

[28] M. H. Fu, Clays and Clay Minerals **38**, 485–492 (1990), ISSN 0009-8604, URL http://dx.doi.org/10.1346/CCMN.1990.0380504.

[29] J. Cases, Clays and Clay Minerals **45**, 8–22 (1997), ISSN 0009-8604, URL http://dx.doi.org/10.1346/CCMN.1997.0450102.

[30] A. Botan, B. Rotenberg, V. Marry, P. Turq, and B. Noetinger, Journal of Physical Chemistry C **114**, 14962 (2010), URL https://hal.science/hal-00531724.

[31] R. Hartkamp and B. Coasne, The Journal of Chemical Physics **141** (2014), ISSN 1089-7690, URL http://dx.doi.org/10.1063/1.4896380.

[32] M. H. Cohen and D. Turnbull, The Journal of Chemical Physics **31**, 1164–1169 (1959), ISSN 1089-7690, URL http://dx.doi.org/10.1063/1.1730566.

[33] K. Falk, B. Coasne, R. Pellenq, F.-J. Ulm, and L. Bocquet, Nature Communications **6** (2015), ISSN 2041-1723, URL http://dx.doi.org/10.1038/ncomms7949.

[34] A. Obliger, R. Pellenq, F.-J. Ulm, and B. Coasne, The Journal of Physical Chemistry Letters **7**, 3712–3717 (2016), ISSN 1948-7185, URL http://dx.doi.org/10.1021/acs.jpclett.6b01684.

[35] R. T. Cygan, J.-J. Liang, and A. G. Kalinichev, The Journal of Physical Chemistry B **108**, 1255–1266 (2004), ISSN 1520-5207, URL http://dx.doi.org/10.1021/jp0363287.

[36] H. J. C. Berendsen, J. P. M. Postma, W. F. van Gunsteren, and J. Hermans, *Interaction Models for Water in Relation to Protein Hydration* (Springer Netherlands, 1981), p. 331–342, ISBN 9789401576581, URL http://dx.doi.org/10.1007/978-94-015-7658-1_21.

[37] W. Smith, C. Yong, and P. Rodger, Molecular Simulation **28**, 385–471 (2002), ISSN 1029-0435, URL http://dx.doi.org/10.1080/08927020290018769.

[38] V. Loskutov and V. Sevriugin, Journal of Magnetic Resonance **230**, 1 (2013), ISSN 1090-7807, URL https://www.sciencedirect.com/science/article/pii/S1090780713000189.

[39] I. Hitchcock, J. A. Chudek, E. M. Holt, J. P. Lowe, and S. P. Rigby, Langmuir **26**, 18061 (2010), pMID: 21043443, https://doi.org/10.1021/la103584k, URL https://doi.org/10.1021/la103584k.

Acknowledgments

This work was supported by OCTAPPOM project in the framework of the research program NEEDS (Nucléaire, Energie, Environnement, Déchets et Société). The authors wish to thank Sachin R. Chaudhari for his help with the NMR experiments.

Authors Contribution

B. C. and D. F. conceived and supervised the research. L. N. H. conducted the molecular simulation task and analyzed the corresponding data. L. N. H., A. R. and A. L. performed the experiments and the corresponding analysis. B. C. developed the theoretical model. B. C. and L. N. H. wrote the manuscript with inputs from all authors.

Competing interests

The authors declare no competing interests.